RSC Sustainability

ROYAL SOCIETY OF CHEMISTRY

PAPER

View Article Online
View Journal | View Issue

Cite this: *RSC Sustainability*, 2024, **2**, 2632

Aloe vera mucilage as a sustainable biopolymer flocculant for efficient arsenate anion removal from water†

Deysi J. Venegas-García, [a] Lee D. Wilson *[a] and Mayela De la Cruz-Guzmán [b]

In recent years, utilization of biopolymers as natural coagulant–flocculant (CF) systems has become an area of interest, due to their sustainable nature (renewable, biodegradable, and non-toxic) and potential utility as alternative systems to replace synthetic flocculants. Herein, a biopolymer extracted from *Aloe vera* mucilage (AVM) was investigated for its arsenic(v) removal properties in a CF water treatment process. Structural characterization of AVM was supported by spectroscopy (FTIR, ^{13}C solids NMR & XPS), TGA, rheology, and pH_{pzc}. The arsenic(v) removal process was optimized by employing the Box–Behnken design under three main factors (coagulant, flocculant dosage and initial arsenic(v) concentration), which led to a reduction of the initial arsenic(v) concentration to levels below the Maximum Acceptable Concentration (MAC; 10 μg L^{-1}). The kinetics and thermodynamics of arsenic(v) removal were analyzed with a one-pot *in situ* method, where the kinetic profiles followed a pseudo-first-order model. The thermodynamic parameters are characteristic of a spontaneous (entropy-driven) and endothermic physisorption removal process. Flocs isolated from the process were analyzed by XPS, where the results reveal that calcium and amide groups of AVM contribute to the arsenic(v) removal mechanism.

Received 9th April 2024
Accepted 19th July 2024

DOI: 10.1039/d4su00170b

rsc.li/rscsus

Sustainability spotlight

Arsenic (As) decontamination of groundwater represents a grand environmental challenge due to its ubiquitous occurrence, high mobility and toxicity, due to concerns over ecosystem and human health. Arsenic "hotspots" possess elevated groundwater concentrations with As-levels above 10 μg L^{-1} that occur across Asia, the America's, and Europe. This research uses *Aloe vera* mucilage as a bioflocculant that reveals unique advantages over other conventional synthetic flocculants. The facile and low-cost bioflocculant-ferric chloride system is suitable for scale-up and implementation in current water treatment technologies for the sustainable treatment of arsenic-laden water to safe levels (below 10 μg L^{-1}). This work contributes to the following UN sustainable development goals: water and sanitation (SDG 6); industry, innovation and infrastructure (SDG 9).

1 Introduction

Adsorption techniques are highly versatile and effective for the removal of various types of contaminants from water. However, the suitability of adsorption as the best method depends on the specific contaminants being targeted and the conditions of the water to be treated.[1–3] The merits of adsorption technology have been described in a recent review by Morin-Crini *et al.*[4] Coagulation–flocculation (CF) is an advantageous method for water treatment due to its efficiency, low cost and technical simplicity.[5] CF is a physico-chemical process that employs the addition of metal ion coagulants (*e.g.*, Al(III) or Fe(III) salts) with complementary charges to neutralize the colloidal particles present in water.[6] Coagulation neutralizes the surface charges of the colloidal particles to enable microfloc formation.[7] Flocculation causes a significant increase in the size and density of the floc particles (macroflocs), which result in a higher sedimentation rate of the particles with phase separation from aqueous media.[8] Upon considering the toxicity disadvantages for the application of synthetic flocculants such as polyacrylamide, there is increasing interest in the utilization of bioflocculants for water treatment. This relates to their beneficial utility over synthetic systems, due to their biodegradability and environmentally benign nature.[9,10] Plant-based biopolymer flocculants generally have a large number of surface charges and adsorption sites that can increase the efficiency of the CF process.[11] Studies focused on the CF activity of natural coagulants/flocculants, such as flaxseed mucilage,[12] chitosan[13,14] and okra mucilage[15] have been reported. Bioflocculants extracted

[a]*Department of Chemistry, University of Saskatchewan, 110 Science Place, Thorvaldson Building (Room 165), Saskatoon, Saskatchewan, S7N 5C9, Canada. E-mail: lee.wilson@usask.ca*

[b]*Universidad Tecnológica de San Luis Potosí, División Industrial, Av. Dr Arturo Nava Jaimes No. 100, Rancho Nuevo, Soledad de Graciano Sánchez, San Luis Potosí, C. P. 78340, Mexico*

† Electronic supplementary information (ESI) available. See DOI: https://doi.org/10.1039/d4su00170b

from *Salvia hispanica*, *Moringa oleifera*, and *Opuntia ficus indica* highlight the treatment of textile leachate and industrial wastewater.[16–18] More recently, a unique bioflocculant such as *Lepidium sativum* mucilage[19] was used for the treatment of suspended matter and heavy metals.

Herein, a biopolymer derived from *Aloe vera* was considered as a potential bioflocculant for the CF treatment of arsenic(v) contaminated water. *Aloe vera* (*Aloe barbadensis* Miller) is a perennial plant in the family *Aloe aceae*,[20] where the main components can be divided into 2 types; namely, aloe latex and aloe gel. Aloe latex is derived from the outer skin of the leaves. Aloe gel, on the other hand, is taken from the inner region of the leaves.[21] *Aloe vera* mucilage (AVM), extracted from *Aloe vera* gel, consists of two main types of polysaccharides: acemannan; β-(1,4)-D-mannosyl units that are acetylated at the C-2 and C-3 positions (Fig. 1). This material is found inside the cells of protoplasts; and a wide variety of polysaccharides that form the network of the cell walls, which is mainly constituted of pectic substances and (hemi)celluloses.[23,24] AVM contains polysaccharides with oxygen-containing functional groups (*e.g.* carboxyl and hydroxyl groups) that can interact with contaminants with complementary donor–acceptor sites, which confers favourable flocculant properties.[25]

The use of different *Aloe vera* components as a bio-coagulant/flocculant for water treatment was reported to reduce water turbidity and oxyanions (nitrate, phosphate) for textile-effluent treatment.[26,27] Bazrafshan *et al.*,[28] reported a low efficiency removal of arsenic(v) *via* a coagulation process with poly-aluminum chloride (PAC), along with the dried leaves of *Aloe vera* as a coagulant aide. Herein, three objectives are addressed: (i) to characterize AVM by FTIR/NMR spectroscopy, TGA, rheology and pH_{pzc}; (ii) to optimize the arsenic(v) removal process though the Box–Behnken design; and (iii) to reveal the adsorption mechanism by kinetic, thermodynamic and XPS characterization of the flocs. This study highlights some distinctive contributions to the field of Environmental chemistry that include the following: (i) to demonstrate the utility of mucilage extracted from *Aloe vera* gel as a bioflocculant for conventional for efficient CF-based removal of arsenic(v) from water, and (ii) to characterize the CF thermodynamics and kinetics of arsenic(v) removal from water, and (iii) to analyse the flocs *via* XPS to gain insight on the arsenic(v) removal mechanism. To the best of our knowledge, this study represents the first report for the removal of inorganic arsenate ions with an AVM system. A key outcome of this study will reveal the utility of AVM for the controlled removal of waterborne arsenate *via* an optimized and sustainable CF process.

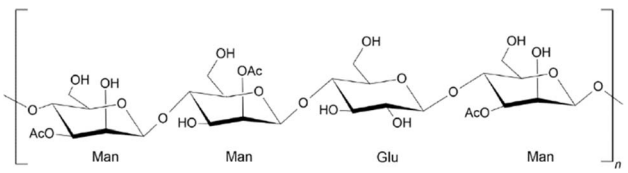

Fig. 1 Chemical structure of acemannan.[22]

2 Materials and methods

2.1 Materials

All chemicals were of analytical reagent (AR) grade. Sodium hydrogen arsenate heptahydrate (98%) was obtained from Alfa Aesar (Tewksbury, MA, USA). Hydrochloric acid (35%), ferric chloride hexahydrate (97%), sodium hydroxide (99%), antimony molybdate tetrahydrate (99.9%), potassium antimony(III) tartrate hydrate (99%), sulfuric acid (98%) and spectroscopic grade potassium bromide (99%) were purchased from Sigma-Aldrich (Oakville, ON, CA). L-Ascorbic acid (99%) was obtained from BDH Chemicals Canada (Mississauga, ON, CA). *Aloe vera* mucilage (AVM) was obtained from the Universidad Tecnológica de San Luis, División Industrial (San Luis Potosí, S. L. P., MX). All materials were used as received unless specified otherwise. Millipore water 18 MΩ cm was used to prepare all stock solutions.

2.2 Fourier transformed infrared (FT-IR) spectroscopy

The FTIR spectra of the flocculants were obtained using a Bio-RAD FTS-40 IR spectrophotometer (Bio-Rad Laboratories, Inc., Philadelphia, PA, USA). Dried powder samples were mixed with pure spectroscopic grade KBr in a 1 : 10 weight ratio with co-grinding in a small mortar and pestle. The Diffuse Reflectance Infrared Fourier Transform (DRIFT) spectra were obtained in reflectance mode at 295 K with a resolution of 4 cm^{-1} over a spectral range of 500–4000 cm^{-1}. Multiple scans were recorded and corrected relative to a spectral reference background of KBr.

2.3 ^{13}C solids NMR spectroscopy

^{13}C solids NMR spectra were obtained with a 4 mm DOTY CP-MAS probe and a Bruker AVANCE III HD spectrometer operating at 125.77 MHz (^{1}H frequency at 500.13 MHz). The ^{13}C CP/TOSS (cross polarization with total suppression of spinning sidebands) spectra were obtained at a sample spinning speed of 7.5 kHz, a ^{1}H 90° pulse of 5 μs with a contact time of 2.0 ms, and a ramp pulse on the ^{1}H channel. Spectral acquisition required *ca.* 2500 scans with a 1 s recycle delay, and a 50 kHz SPINAL-64 decoupling sequence. ^{13}C NMR chemical shifts were externally referenced to adamantane at 38.48 ppm (low field signal).

2.4 Thermogravimetric analysis (TGA)

Thermogravimetric (TG) weight loss profiles of AVM were obtained using a TA Instruments Q50 TGA system (New Castle, DE, USA) with a heating rate of 5 °C min^{-1} up to 500 °C, where nitrogen was the carrier gas. The TG profiles are shown as first derivative TG plots (DTG) of weight with temperature (%/°C) against temperature (°C).

2.5 pH at the point-of-zero-charge (pH_{pzc})

The pH at the point-of-zero-charge (pH_{pzc}) for AVM was determined according to a method described by Kong & Wilson.[29] A stock solution of NaCl (0.01 M) was prepared and 20 mL portions were added into five vials (8 dram). The solution pH

conditions of the samples were adjusted between pH 1 to 8 using NaOH (aq) or HCl (aq) media. The AVM flocculant (50 mg) was added to each solution and allowed to equilibrate for 48 h before the final pH was recorded. The pH_{pzc} was estimated plotting change in pH (ΔpH) against initial pH, and the point of intersection of the resulting null pH refers to the point zero charge (pH_{pzc}).

2.6 Rheological measurements

The viscosity of the AVM dispersion was determined using an AR G2 rheometer (TA Instrument, Montréal, QC, Canada) equipped with a Peltier temperature controller (Smart Swap™, TGA Heat Exchanger, TA Instrument, Montréal, QC, Canada) for maintaining constant temperature (25 ± 0.2 °C). The oscillatory shear/strain was applied to the sample using a 40 mm diameter and 2° acrylic cone geometry. The gap between the rotational and stationary plate was set to 1000 μm. During each measurement, samples were equilibrated for 120 s. The apparent viscosity of the gum dispersion was measured as a function of shear rate ranging from 0.01 to 1000 s^{-1}. The rheometer was operated in the oscillatory mode to determine the dispersion viscoelastic behaviour, where the storage (G') and loss (G'') moduli were measured as a function of strain (0.01–1000%) at a constant frequency (6.28 rad s^{-1}).

The intrinsic viscosity of AVM dispersions was determined at diluted AVM concentrations ranging from 0.1 to 0.25 wt% in $NaNO_3$ (0.1 M). For the determination of intrinsic viscosity, the apparent viscosity (η) of the AVM dispersion was converted to relative viscosity (η_{rel}) using eqn (1):

$$\eta_{rel} = \frac{\eta}{\eta_s} \quad (1)$$

where η_s is the solvent viscosity. Intrinsic viscosity ($[\eta]$) is obtained by extrapolation of the natural log of η_{rel}/c to zero concentration, according to the Kraemer empirical equation (eqn (2)) as follows:

$$\frac{\ln \eta_{rel}}{c} = [\eta] + k[\eta]^2 c \quad (2)$$

where k and c are the respective Kraemer constant and solute concentration. Once the $[\eta]$ was calculated, the viscosity average molecular weight (M_v), was calculated using modified Mark–Houwink[30] relationship *via* eqn (3).

$$[\eta] = K(M_v)^a \quad (3)$$

where K and a are the Mark–Houwink parameters for AVM in solution.[30,31]

2.7 Coagulation–flocculation process

The coagulation–flocculation parameters were based on the experimental design matrix obtained from the BBD and the RSM, using a program-controlled conventional jar test Phipps & Bird PB-900 apparatus (Richmond, VA, USA) with six 2 L jars and stirrers. Approximately 1 L of simulated arsenic(v)-containing sample (0.5, 2.75 or 5 mg L^{-1}) was added to the jar tester vessel and the pH was adjusted using 0.1 M NaOH or 0.1 M HCl to pH 7.5 ± 0.1. An aliquot of the arsenic(v) solution was sampled to measure the initial concentration ($[As]_0$). The CF process was carried out by adaptation of a reported method.[32] A predetermined amount of Fe^{3+} salt (1, 5.5 or 10 mg L^{-1}) was added to the solution, followed by rapid stirring for 3 min at 295 rpm. Then, the stirring rate was reduced to 25 rpm for 20 min. During this period, the bioflocculant (0.5, 10.25 or 20 mg L^{-1}) was added within the first 5 min. Then, the stirring was stopped and a settling time of 90 min was employed. For arsenic(v) quantification, 3 mL of sample was used for UV-vis spectral analysis by adding 0.5 mL of molybdate reagent.[33] After addition of the reagent to the arsenic(v) sample, a blue coloured complex formed after 20 min before the UV-vis absorbance values were recorded. A calibration curve of arsenic(v) was obtained using the molybdate colorimetric method (λ = 900 nm) with a SPECTRONIC 200 Visible Spectrophotometer (**https://www.thermofisher.com/order/catalog/product/714-039400?icid=MSD-SPEC-UVComparisonGuide**) (Waltham, MA, USA). Experiments were carried out in duplicate, where the average values are reported. The removal efficiency (RE; %) of arsenic(v) and the arsenic(v) adsorption capacity (q_e; mg g^{-1}) were obtained by eqn (4) and (5), respectively.

$$RE(\%) = \frac{C_0 - C_e}{C_0} \times 100 \quad (4)$$

$$q_e = \frac{(C_0 - C_e) \times V}{m} \quad (5)$$

Here, C_0 and C_e are the initial and equilibrium concentrations (mg L^{-1}) of arsenic(v), V is the solution volume (L), and m is the total weight (g) of the coagulant–flocculant (CF) system.

2.8 Box–Behnken experimental design

The BBD method was used to determine the effects of key operational variables on the arsenic(v) removal and to empirically determine the combined variables that yield the maximum arsenic(v) removal. The BBD is a response surface methodology, which is a collection of mathematical and statistical techniques that are useful for the modelling and analysis of systems, where a response of interest is influenced by several variables, and the goal is to optimize the overall response.[34] Preliminary experiments indicate that three important operating parameters in the CF process that govern arsenic(v) removal include coagulant dose, flocculant dose and $[As]_0$. These variables were chosen as the independent variables and designated as A, B and C, respectively. Coagulant dose (A) was varied between 1 to

Table 1 Levels of each independent factor for the Box–Behnken design method

			Coded levels		
Independent factors	Units	Symbol	−1	0	1
Coagulant	mg L^{-1}	*A*	1	5.5	10
Flocculant	mg L^{-1}	*B*	0.5	10.25	20
Arsenic(v)	mg L^{-1}	*C*	0.5	2.75	5

10 mg L^{-1}, flocculant dose (B) was varied between 0.5 to 20 mg L^{-1} and $[As]_0$ (C) varied from 0.5 to 5 mg L^{-1}. In Table 1, the experimental design involved the three parameters (A, B and C), each at three levels, coded −1, 0, and +1 for low, middle, and high concentrations, respectively.

To correlate the arsenic(v) removal efficiency (Y) with other independent variables (A, B and C), a response surface function was utilized (eqn (6)). Where Y is acting as the predicted response surface function, b_0 is the model constant, b_1, b_2 and b_3 linear coefficients, whereas b_{12}, b_{13}, and b_{23} are the cross product coefficients, and b_{11}, b_{22}, and b_{33} are the quadratic coefficients in eqn (6).

$$Y = b_0 + b_1A + b_2B + b_3C + b_{12}AB + b_{13}AC + b_{23}BC + b_{11}A^2 + b_{22}B^2 + b_{33}C^2 \quad (6)$$

The response function coefficients were determined by regression analysis of the experimental data and the Minitab 19 DOE regression program.

2.9 Kinetic studies

The adsorption of arsenic(v) onto the surface of adsorbent (Fe^{3+}-AVM) is a dynamic process, where the kinetic profile for the CF process reflects the change in the adsorption rate and time with the environmental conditions. Kinetic adsorption models such as the pseudo-first order (PFO) and pseudo-second order (PSO) models were used to examine the arsenic(v) adsorption data. The non-linear forms of the PFO and PSO models are defined by eqn (7) and (8), respectively:

$$q_t = q_e(1 - \exp^{-k_1 t}) \quad (7)$$

$$q_t = \frac{q_e^2 k_2 t}{1 + q_e k_2 t} \quad (8)$$

q_t (mg g^{-1}) and q_e (mg g^{-1}) indicate that the adsorption capacity of Fe^{3+}-AVM floc towards arsenic(v) at time (t), and at equilibrium. k_1 (min^{-1}), and k_2 (g mg^{-1} min^{-1}) are the respective rate constants for the PFO and PSO models.

Kinetic studies were performed using the one-pot method, as described by Mohamed & Wilson.[35] Briefly, a 600 mL beaker with 500 mL of arsenic(v) solution was mixed by magnetic stirring. A filter paper (Whatman no. 40) was folded into a cone and attached to the beaker that was immersed in the solution at a depth of 2 cm whilst stirring at 25 rpm (*cf.* Fig. 2). Sampling of aliquots (3 mL) within the inner filter cone began at zero time (t = 0), when the CF system was added, sampling continued at 1 min intervals for 10 min, then for a further 10 min at 2 min intervals, and finally for 40 min at 5 min intervals. At this point, stirring was stopped after 60 min (t = 60) and sampling continued for an additional 40 min at 10 min intervals. Sample aliquots were prepared for UV-vis spectral analysis, as discussed above, where the arsenic(v) adsorption capacity (q_t) at variable time intervals was determined by eqn (5).

Additionally, the Weber–Morris intraparticle diffusion model was used to investigate the rate-limiting step of arsenic(v) adsorption, as defined by eqn (9):[36]

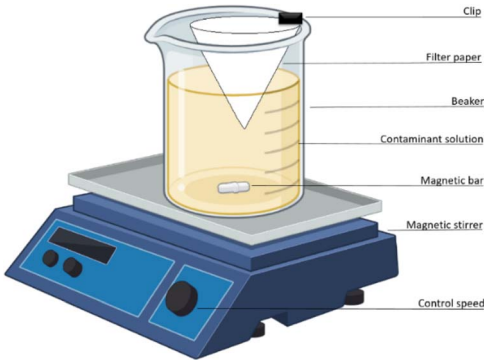

Fig. 2 Diagram for the one-pot kinetic system.

$$q_t = kt^{0.5} + C \quad (9)$$

where C represents the intercept, $t^{0.5}$ is the square root of the contact time, and k is the kinetic rate constant. Adsorption dynamics include three consecutive steps, as follows: (i) boundary diffusion, where adsorbate diffuses onto the external adsorbent surface; (ii) intraparticle diffusion into the pores of the adsorbent; and (iii) adsorbate binding occurs within the matrix of the adsorbent.[37]

2.10 Thermodynamics of adsorption

Thermodynamic adsorption parameters such as enthalpy and entropy changes govern the Gibbs energy of the adsorption process that allow for prediction of the degree of spontaneity at variable temperature. Thermodynamic isotherm parameters were evaluated for arsenic(v) adsorption include the standard difference in Gibbs energy (ΔG°), according to eqn (10):

$$\Delta G^\circ = -RT \ln K_e \quad (10)$$

where $K_e = q_e/C_e$; refers to the thermodynamic equilibrium constant (K_e; L g^{-1}); q_e is the amount of arsenic(v) adsorbed per unit mass of the adsorbent (mg g^{-1}) that is scaled to the arsenic(v) content; C_e is the equilibrium concentration of arsenic(v) in solution (mg L^{-1}); R is the universal gas constant (8.314 J mol^{-1} K^{-1}); T is the temperature in Kelvin (K). Based on eqn (10), ΔG° can be calculated and then partitioned into the enthalpy (ΔH°) and entropy (ΔS°) terms, according to eqn (11):

$$\Delta G^\circ = \Delta H^\circ - T\Delta S^\circ \quad (11)$$

Substituting eqn (10) into eqn (11), and re-arrangement yields eqn (12),

$$\ln K_e = -\frac{\Delta H^\circ}{RT} + \frac{\Delta S^\circ}{R} \quad (12)$$

where the values of ΔH° and ΔS° were determined from the slope and intercept of a linear plot of ln K_e *versus* $1/T$, according to eqn (12).[38]

2.11 Optical microscopy

Samples of isolated wet flocs were deposited onto a microscope slide for analysis using optical microscopy. To avoid any undue

mechanical forces on the samples, which may affect the floc structure because of compression, and no cover slips were used. Optical images of the flocs were captured on a Renishaw InVia Reflex Raman microscope (Renishaw plc, New Mills, UK) with 5× magnification.

2.12 X-ray photoelectron spectroscopy (XPS)

All X-ray Photoelectron Spectroscopy (XPS) measurements were collected using a Kratos (Manchester, UK) AXIS Supra system at the Saskatchewan Structural Sciences Centre (SSSC) under UHV conditions. This system is equipped with a 500 mm Rowland circle monochromated Al K-α (1486.6 eV) source and combined hemi-spherical analyzer (HSA) and spherical mirror analyzer (SMA), where a spot size of 300 × 700 microns was employed. All survey scan spectra were collected in the −5–1200 binding energy range in 1 eV steps with a pass energy of 160 eV. High resolution scans of 4 regions were also conducted using 0.1 eV steps with a pass energy of 20 eV. An accelerating voltage of 15 keV and an emission current of 10 mA were used for the analysis. Data processing was carried out with the Casa XPS software.[39] The spectra were calibrated against adventitious carbon at 284.8 eV.

3 Results and discussion

As discussed above in the Introduction (*cf.* Section 1), several objectives were outlined and the corresponding results are presented in the following section. The first part of Section 3 describes the structural characterization of AVM, followed by the physico-chemical characterization of AVM that are relevant to the arsenic(v) adsorption properties, where the final part of Section 3 describes the CF results under equilibrium and kinetic conditions.

3.1 FTIR spectroscopy results

The main functional groups of AVM were identified using FTIR spectroscopy. The IR spectrum (Fig. 3a) presents a broad band in the 3316 cm^{-1} region that relates to the vibrational stretching and hydrogen bonding of the –OH groups. The bands in the region of 2930 and 2897 cm^{-1} are attributed to the aliphatic C–H stretching vibrational bands. The IR signature at 1742 cm^{-1} is attributed to the carbonyl stretching (C=O) band. In addition, the band 1433 cm^{-1} is characteristic of the symmetric stretching vibration of a carboxylate group (COO^-). Bands at 1375 and 1242 cm^{-1} are related to the respective C–N stretches of amide III and C–O–C stretching vibrations of acetyl groups for the acetylated polysaccharide acemannan.[40] The bands in the region of 1084 to 1041 cm^{-1} are mainly attributed to polysaccharides with galactose and glucan. The overlapping absorption bands in the region 1599 to 1651 cm^{-1} are attributed to carboxyl asymmetrical stretching of the COO^- group or N–H amide vibrations, due to the presence of residual proteins in AVM.[41,42] The existence of key functional groups (–COOH and –OH) in AVM (*cf.* Fig. 1) are inferred to play a key role concerning its effective application as a biopolymer flocculant. The spectral results are in good agreement with previous reports for characterization of the structural features of AVM.[43,44]

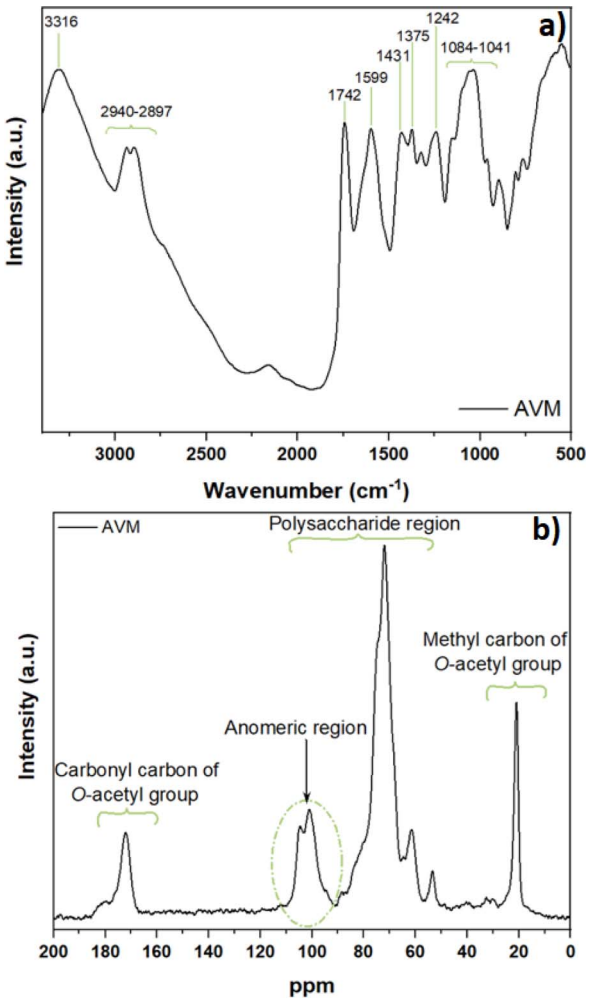

Fig. 3 Spectral results for *Aloe vera* mucilage: (a) FTIR spectrum and (b) solid state ^{13}C NMR spectrum obtained at 295 K.

3.2 ^{13}C solids NMR spectroscopy

Fig. 3b shows the solids ^{13}C NMR spectrum for *Aloe vera* mucilage, were the anomeric signal at 100.2 ppm, is attributed to C-1 of the β-mannopyranosyl units. The signature at 102.5 ppm indicates the presence of 4-linked β-glucopyranosyl units. ^{13}C NMR lines for the methyl carbons at 20.8 ppm and carboxyl carbons (173.8 ppm) of acetyl groups support that AVM contains acetylated mannan.[45] The small overlapping NMR line near 180 ppm may originate from carboxylate as evidenced in the FT-IR spectrum (*cf.* Fig. 3a and the IR band at 1433 cm^{-1}). NMR lines between 55 to 110 ppm are attributed to the polysaccharide spectral region that is characteristic of glucomannan.[46] The presence of protein in *Aloe vera* is supported by the ^{13}C NMR signatures between 25 ppm to 70 ppm, ascribed to C–N from amides.[47] The NMR results presented herein are also corroborated by independent studies.[48,49]

3.3 Thermogravimetric analysis

Fig. 4a provides insight on the thermal stability *versus* temperature, as revealed by the TG profile and its first derivative *versus* temperature for AVM. Based on the DTG profile (*cf.* Fig. 4a, green)

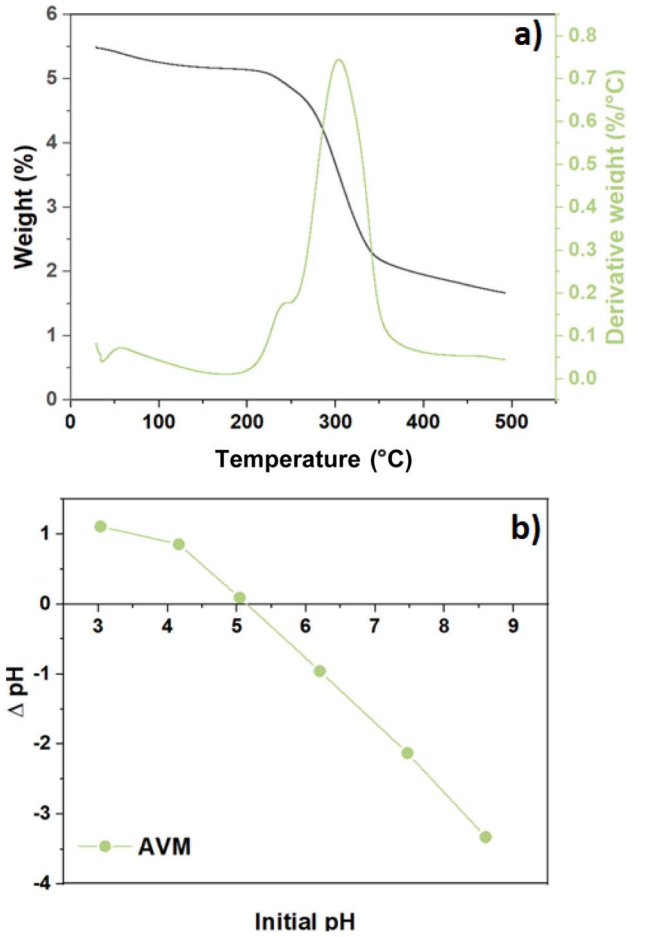

Fig. 4 (a) weight loss profiles are presented as a DTG profile (green) and TG weight loss *versus* temperature (black) and (b) zero-point-charge (pH_{pzc}) as a function of change on pH *vs.* variable initial pH for *Aloe vera* mucilage (AVM).

and TG profile (Fig. 4a, black), three distinct weight loss regions are observed that relate to characteristic thermal weight loss events. Below 150 °C, physisorbed water and/or low molecular weight volatile compounds and evolved gases or volatiles are released. Between 150 °C to 250 °C, weight loss occurs due to loss of low molecular weight compounds such as surface functional groups. Above 250 °C, the carbon framework of the polysaccharide undergoes decomposition between the onset and final temperature. AVM shows a maximum weight loss near 300 °C up to a final temperature of decomposition near 350 °C.[50]

3.4 pH_{pzc}

The pH_{pzc} parameter indicates the pH where the net surface charge of a material is zero, which also provides insight on the role of electrostatic effects between the flocculant material surface with charged species, according to the pH of the media. The surface charge of the adsorbents is negative when the solution pH is above pH_{pzc}, where the adsorption of cation species is favoured due to deprotonation of the flocculant acidic surface sites to yield a negative surface charge. Meanwhile, at pH values below the pH_{pzc}, a positive surface charge prevails, where adsorption of OH^- ions and other anionic species occur. This trend concurs with a positive ζ-potential of the sorbent at $pH < pH_{pzc}$. Fig. 4b shows that the pH_{pzc} value for AVM is 5.15, in agreement with another *Aloe vera* study.[51]

3.5 Intrinsic viscosity and viscosity average molecular weight

The intrinsic viscosity ($[\eta]$) provides an approximation of the molecular conformation of the biopolymer and its interactions with the aqueous media. Kraemer's plot provides the intrinsic viscosity of AVM (Fig. S1, ESI†). Kraemer's model (eqn (2)) provides a good fit to the experimental results with a favourable statistical correlation ($R^2 = 0.98$). The intrinsic viscosity of AVM dispersions was calculated from the *y*-intercept of Fig. S1 (*cf.* ESI†) where $[\eta] = 20.8 \pm 0.3$ dL g^{-1}.[31] The average viscosity-based molecular weight was estimated using the intrinsic viscosity of AVM *via* the modified Mark–Houwink relationship (eqn (3)). The AVM average viscosity molecular weight (M_v) calculated herein was $26 \pm 1.4 \times 10^6$ g mol^{-1}. In comparison with other studies, the average viscosity-based molecular weight of AVM agrees favourably with the intrinsic viscosity value reported herein.[52,53]

3.6 Box–Behnken experimental design (BBD)

3.6.1 Main effects of independent variables on the response functions. The removal of arsenic(v) (RE; %) from water was explored by a CF process, which considers the role of three key operating parameters (coagulant dose, flocculant dose and initial arsenic(v) concentration) by the BBD method. The statistical significance of the response function generated was verified by the *F*-test and ANOVA results (*cf.* Table S1, ESI†). Factors that have a *p*-value < 0.05, which indicate statistical significance. Plots depicting the main effects for the arsenic(v) removal efficiency are presented in Fig. S2 (*cf.* ESI†). These plots illustrate important factors that are set at three levels for the designed experiment, which enable an in-depth analysis of the effects of factors on the CF process. These plots provide a preliminary estimate on the effects of independent variables (coagulant dose, flocculant dose and $[As]_0$) on the response (RE; %). The effect of increasing coagulant dosage from 1 to 10 mg L^{-1} (*cf.* Fig. S2a, ESI†) shows that the arsenic(v) removal (RE; %) increases with greater coagulant dosage. The RE value reaches a maximum *ca.* 88% with 5.5 mg L^{-1} of Fe^{3+}, in agreement with other studies that employ $FeCl_3$ as the coagulant.[54,55] The initial arsenic(v) concentration (*cf.* Fig S2c, ESI†), has statistical significance as the main factor, square and 2-way interaction with coagulant dosage with *p*-values < 0.05. The arsenic(v) RE (%) increases (50 to 93%) as the $[As]_0$ increases from 0.5 to 3 mg L^{-1}. When the value of $[As]_0$ increases beyond 3 mg L^{-1}, the RE (%) shows a decrease from 93 to 80%. These results corroborate the formation of As–Fe oxides complexes as the rate determining step in the process.[56] The role of the flocculant dosage from 0.5 to 20 mg L^{-1} (*cf.* Fig. S2b, ESI†) exhibited a variation from *ca.* 93 to 97% of arsenic(v) removal. According to the *F*-test, the flocculant dosage has no statistical significance as the main factor, square or 2-way interaction, with *p*-values > 0.05. In order to explore the interactions of various major

Table 2 Optimization for arsenic(v) removal (RE; %)

Coagulant (mg L^{-1})	Flocculant (mg L^{-1})	Arsenic(v) initial concentration (mg L^{-1})	RE (%) predicted	RE (%) experiment
5.5	20	3.33	99.1	99.7[a]

[a] Below of limit of detection (10 μg L^{-1}).

operating factors on arsenic(v) removal by the CF process, the Response Surface Methodology (RSM) was employed. Contour plots (*cf.*, Fig. S3–S5; ESI†) were obtained from the model-predicted response by changing two independent variables within the experimental conditions at the same time, whereas the third variable was fixed at a constant optimal level. These plots are useful to assess the interactive relationship between the independent variables and the response variable.

3.6.2 Box–Behnken analysis. The coefficients of the response function for arsenic(v) RE (%) are presented in Table S2 (*cf.* ESI†). The coefficient of determination (R^2) values for the system was 0.93, showing evidence of a good correlation. A response optimization was achieved for the process, determined by the response models for the experimental data. Table 2 lists the optimal parameters and the confirmation of the results, where the predicted *vs.* the experimental results show favourable agreement. The corresponding predicted arsenic(v) removal (RE; %) at optimal experimental conditions was 99.08%. The optimized conditions indicate a dosage of Fe^{3+} (5.46 mg L^{-1}) resulted in an optimal level of arsenic(v) removal, where the concentration of AVM was 20 mg L^{-1} for an $[As]_0$ of 3.33 mg L^{-1}.

Additional comparison of arsenic(v) removal through various coagulants and flocculants is outlined in Table 3 below, where a comparison of the results for the Fe^{3+}-AVM in this study with other biopolymer systems reveals comparable RE (%) for arsenic(v).[12,28,57–60,62]

3.7 Coagulation–flocculation kinetics

To study the effect of the system Fe^{3+}-AVM for arsenic(v) removal, the one-pot kinetic experiment was employed. Table 4 summarizes the kinetic parameters obtained for arsenic(v) adsorption. In Table 4, an improved fit ($R^2 = 0.96$) was obtained by the PFO model over the PSO model ($R^2 = 0.94$). In turn, the CF process is inferred to depend on the initial As(v) concentration ($[As]_0$), which concurs with other reports revealing that $[As]_0$ is the main factor governing the kinetics of the CF process.[61,63] The PFO model for describing arsenic(v) uptake by Fe^{3+}-AVM system concurs with the kinetic results with other biopolymer systems reported elsewhere.[64]

The kinetic behavior of the system Fe^{3+}-AVM for the removal of arsenic(v) is shown in Fig. 5, where the kinetic models (PFO and PSO), along with particle and intraparticle diffusion (IPD) contributions[65,66] that were used to fit the adsorption profiles for arsenic(v) removal *versus* time. The adsorption process of

Table 3 Comparison of maximum RE (%) of arsenic(v) in aqueous media for different biopolymer flocculant systems

Flocculant	Concentration (mg L^{-1})	Coagulant	Concentration (mg L^{-1})	As(v) (mg L^{-1})	pH	RE (%)	Reference
Aloe vera powder	2	PAC	3	0.2–1	5	92.6	28
Chitosan	0.5	$FeCl_3$	15–30	0.2–2	7	~100	57
Opuntia ficus indica gum	350	—	—	0.002–0.01	5.9	70	58
—	—	$FeCl_3$	27	1	5	98	59
—	—	$Fe_2(SO_4)_3$	100	5	6	99	60
—	—	$Al_2(SO_4)_3$	25–50	0.065–0.216	7–8	81	61
Flaxseed gum	60–64	$FeCl_3$	35–36	50	7–7.5	77–90	12
Fenugreek gum	52–62	$FeCl_3$	32–33	50	7–7.5	69–90	12
Xanthan gum	37–50	$FeCl_3$	34	50	7–7.5	70–93	12
Aloe vera mucilage	5.5	$FeCl_3$	20	3.33	7.5	99.7	This work

Table 4 Adsorption kinetics parameters based on the pseudo-second order (PSO) and pseudo-first order (PFO) models for arsenic(v) adsorption by the Fe^{3+}-AVM system at 296 K

	PFO model			PSO model		
CF system	k_1 (min^{-1})	q_e (mg g^{-1})	R^2	k_2 (mg g^{-1} min^{-1})	q_e (mg g^{-1})	R^2
AVM	0.046	189.7 ± 8.8	0.96	1.39×10^{-4}	261.2 ± 22.0	0.94

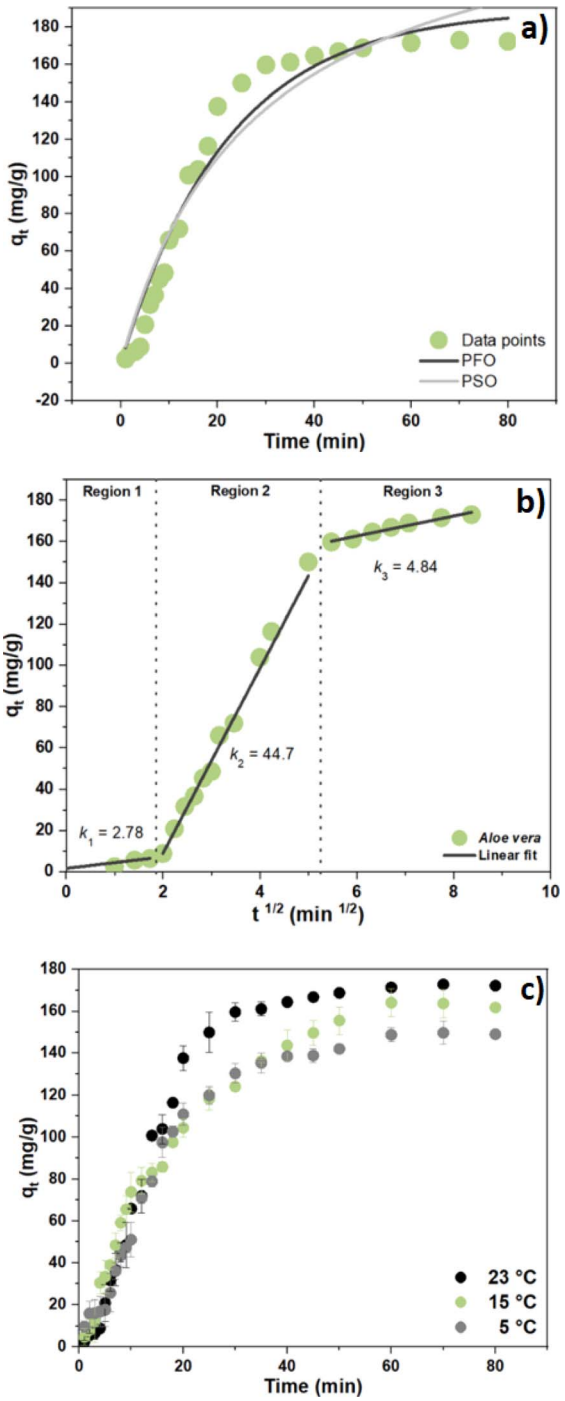

Fig. 5 (a) Kinetic uptake profiles for arsenic(v) anion with the Fe^{3+}-AVM system at pH 7.5 and 23 °C, (b) linear fit of the three regions and intraparticle diffusion model and (c) adsorption process *via* kinetic adsorption profiles at 5, 15 and 23 °C.

arsenic(v) by the Fe^{3+}-AVM system is divided into two parts: (i) a fast-initial adsorption stage, where *ca.* 90% of the adsorption capacity was achieved, and (ii) a subsequent slow adsorption phase, where the adsorption profile followed the PSO model (Fig. 5a).

Fig. 5b shows a multi-linear segmented profile of arsenic(v) adsorption by the Fe^{3+}-AVM system, which supports that the overall adsorption process follows three steps. Specifically, the slope of each linear segment in the plot determines the rate of adsorption, where a higher slope indicates a more rapid adsorption process. As shown in Fig. 5b, the k_2 value (2nd step) was significantly higher than the values for k_1 and k_3 (1st/3rd steps), indicating that the IPD process was the rapid step and boundary diffusion as the rate determining step. Fig. 5c presents the effect of temperature (5, 15 and 23 °C) on the kinetics for arsenic(v) removal. Kinetic results showed that by decreasing the temperature from 23 °C to 5 °C, the adsorption capacity decreased from 170 to 140 mg g^{-1}. As the temperature decreases, floc aggregation tends to be reduced, according to the attenuated motional dynamics of the system and that the more favourable hydration of AVM.[67] This leads to fewer particle–particle collisions where the collision energy is low or attenuated due to enhanced hydration of the AVM biopolymer at lower temperature, along with decreased coagulation efficiency.[68]

3.8 Thermodynamics of the adsorption process

To gain insight on the role of temperature for the arsenic(v) adsorption by the Fe^{3+}-AVM system, adsorption experiments were carried out at variable temperature conditions. The corresponding thermodynamic parameters ($\Delta G°$, $\Delta S°$ and $\Delta H°$) were estimated between 23 °C to 5 °C by employing a van't Hoff graphical analysis. The van't Hoff plot is shown in Fig. S6 (ESI†). Table 5 shows the thermodynamic parameters ($\Delta G°$, $\Delta S°$ and $\Delta H°$) for the adsorption process, where a negative value of $\Delta G°$ indicates the spontaneous nature of the arsenic(v) removal during the CF process. The arsenic(v) adsorption is favourable but reveals a decrease at lower temperatures. Negative $\Delta G°$ values with greater magnitude indicates a greater driving force for adsorption, where attenuation of arsenic(v) adsorption occurs at lower temperature.[69] A positive value for $\Delta H°$ confirms that the process is endothermic and entropy-driven.[70]

The predominance of physical adsorption was verified by the magnitude of $\Delta H°$ (31.61 kJ mol^{-1}). According to Ohale *et al.*,[71] a physisorption process is favoured when $\Delta H°$ is below 80 kJ mol^{-1}. Moreover, the degree of randomness enhanced through the adsorption system, exposed by the positive $\Delta S°$ value.

Table 5 Thermodynamic parameters for arsenic(v) removal through Fe^{3+}-AVM system

Temp. (K)	(1/*K*)	C_e	q_e (mg g^{-1})	k_e (L g^{-1})	ln k_e	$\Delta G°$ (kJ mol^{-1})	$\Delta H°$ (kJ mol^{-1})	$\Delta S°$ (J K mol^{-1})
295.15	0.0034	0.72	172.20	239.16	5.47	−13.47	31.61	152.22
288.15	0.0035	0.96	161.83	168.57	5.12	−12.25		
278.15	0.0036	1.43	149.10	104.26	4.64	−10.73		

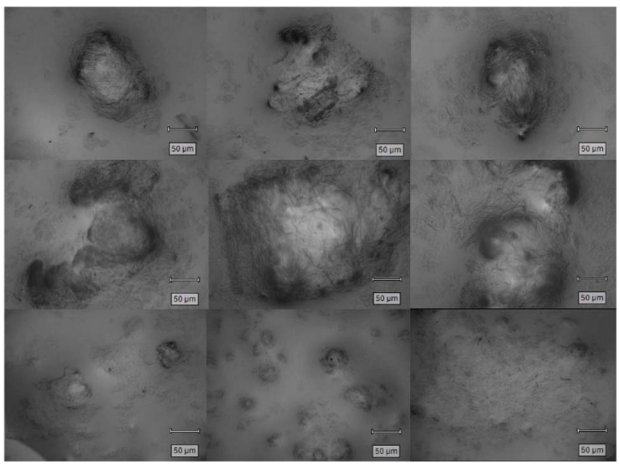

Fig. 6 Flocs microscopy images after the arsenic(v) removal process with the Fe^{3+}-AVM system, 5× magnification.

3.9 Floc characterization

3.9.1 Floc images. To obtain further insight on the macroscopic characteristics of the flocs, the solid flocs were collected from the bottom of the jar test beaker after the CF process and rinsed with Millipore water. Some notable features can be appreciated from the optical microscopy images obtained (*cf.* Fig. 6), where irregular and polyhedral shapes with variable diameters observed in the aggregated flocs.

3.9.2 XPS analysis. Elemental analysis employed XPS, where the characteristic binding energies for each element affords unequivocal elemental identification present in the bound state on the bioflocculant surface (*cf.* Fig. 7). Due to sufficient penetration of X-rays through the finely powdered samples, the surface sensitivity of this technique was used to estimate the bulk composition of the AVM and the flocs formed during the CF process for arsenic(v) removal. Fig. 7 (green) shows the assigned peaks for C 1s, O 1s and N 1s detected near 285, 532 and 400 eV for AVM, respectively. The C 1s spectrum was deconvoluted into four bands (*cf.* Fig. S7, ESI†) with variable binding energies: of 284.8 (C–C), 286.50 (C–OH/C–O–C), 288.02 (C═O) and 289.23 eV (–COOH), where the assignment is listed in parentheses. The signal for N 1s in AVM, confirms the presence of proteins that is corroborated by the IR signals for amide groups.[72,73] The N 1s spectrum of AVM was deconvoluted into three bands (*cf.* Fig. S8, ESI†) with variable binding energy (399.78 and 400.66 eV), ascribed to amide (N(C═O)–), whereas the band at 401.87 eV relates to contributions from the residual $–NH_3^+$ group on the AVM surface.[74] The XPS band for Ca 2p was detected near 347 eV, which concurs with a report for the mineral content of *Aloe vera*.[75] The XPS spectrum of the flocs formed after the CF process (*cf.* Fig. 7, black) show the assigned XPS bands for C 1s (285 eV), O 1s (532 eV), N 1s (400 eV), and Ca 2p (343 eV). As well, the bands for Na 1s (1071.41 eV), Fe 2p (712.72 eV) and As 3d (46 eV) were also detected. Deconvoluted XPS spectra for C1s and N 1s are presented in Fig. S9 and S10 (*cf.* ESI†), where no appreciable changes were observed after adsorption of As(v). The binding energy for Ca 2p reveals a band shift from 347.39 to 343.41 eV after the floc formation, which may indicate a contribution from calcium bridging in the arsenic(v) removal process.[76,77] The XPS band ascribed to Na 1s can be explained through the addition of NaOH and Na_2HAsO_4 during the experiment. The presence of Fe is attributed to the FeOOH formation during the CF process. Fig. S11 (*cf.* ESI†) shows that the deconvoluted band concurs with FeOOH. The surface of the flocs formed during the process showed the presence of arsenic(v) on the adsorbent surface, which corroborates the removal of arsenic(v) during the floc formation process. The deconvoluted peak splitting is shown in Fig. S12 (*cf.* ESI†).

In addition, Table 6 shows the binding energy and atom content (%) for the elements present in the AVM and in the flocs after the CF process. The atom content (%) for C 1s decreased from 63.83 to 41.35%, while O 1s, N 1s and Ca 2p underwent an increase. O 1s increased from 34.73 to 38.47%, due to the FeOOH formation that suggests an arsenic(v) removal contribution upon floc formation. The atom content (%) is

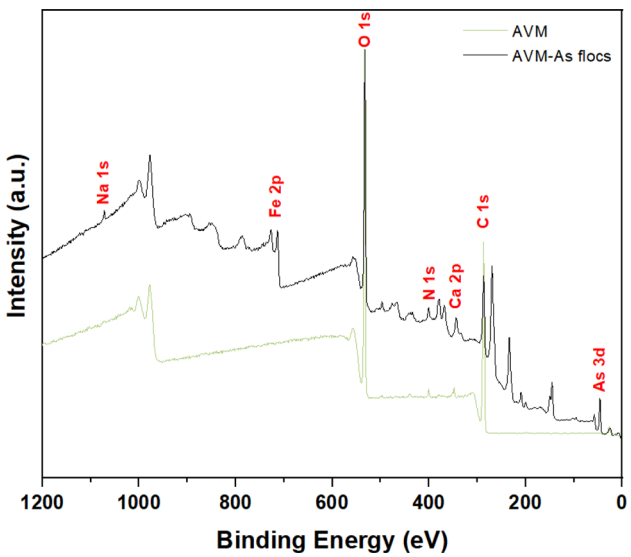

Fig. 7 XPS spectra for AVM and flocs formed for arsenic(v) removal.

Table 6 Binding energy (BE) and atom content (%) present on the AVM biopolymer surface after floc formation during arsenic(v) removal

	AVM		AVM-As(v) flocs	
Element	BE[a] (eV)	Atom content (%)	BE (eV)	Atom content (%)
C	286.5	63.8	286.5	41.3
O[b]	533	34.7	533	38.5
N	400	0.9	400	3.6
Ca	347	0.5	343	2.9
Fe	No signal	0	712	5.6
As(v)	No signal	0	145	6.6
Na	No signal	0	1071.4	0.5

[a] Envelope maxima used in the table (rounded). [b] No narrow scan provided.

incremental for N 1s (from 0.96 to 3.67%), which supports higher protein content in flocs, along with the role of amide groups in the arsenic(v) removal mechanism. Further, the identified narrow scan for arsenic(v) (*cf.* Fig. S12, ESI†) showed a signal at 45.98 eV, indicating As–O speciation congruent with As(v).[78] Finally, the Ca 2p atom content (%) increased from 0.48 to 2.90%, which corroborates a contribution due to a bridging mechanism for arsenic(v) removal, as reported previously.[77]

4 Conclusions

Characterization of AVM through complementary techniques provided insight on the structure–function relationship of the biopolymer coagulation–flocculation (CF) process for removal of arsenic(v). The presence of key functional groups in AVM (–COOH and –OH) are highly significant concerning its effective application as a biopolymer flocculant for arsenic(v) removal in the CF process, along with an iron-based coagulant. A Box–Behnken statistical experimental design was employed to optimize the coagulant dosage, flocculant dosage and initial arsenic(v) concentration for the arsenic(v) removal (RE; %). To achieve a maximum value of RE of 99.1%, the following optimized conditions were used: $FeCl_3$ coagulant dosage (5.5 mg L^{-1}), AVM flocculant dosage (20 mg L^{-1}), and initial arsenic(v) concentration (3.33 mg L^{-1}). The removal of arsenic(v) followed the PFO kinetic profile, where the rate determining step was related to intra-particle diffusion. Variable temperature kinetic profiles revealed a decreasing removal from 170 mg g^{-1} to 140 mg g^{-1}, revealing that the CF process was physisorption in nature. The CF removal process was spontaneous and entropy-driven due to its endothermic (ΔH° = 31.6 kJ mol^{-1}) nature. Interestingly, the XPS results revealed that the amine and calcium content are enriched in the flocs *versus* the raw materials, indicating the role of Ca^{2+} bridging in the arsenic(v) removal mechanism. This study demonstrates that *Aloe vera* mucilage offers a sustainable and efficient bioflocculant alternative (*cf.* Table 3) for the controlled removal of arsenic(v) from water to provide safe levels (10 μg L^{-1}) below the WHO guideline. Further research will focus on the application of AVM relevant to wastewater and groundwater samples that examine the arsenate and arsenite removal at variable conditions.

Data availability

The data supporting this article have been included as part of the ESI.†

Author contributions

Conceptualization, D. J. V.-G., and L. D. W.; methodology, D. J. V.-G. and M. D. l. C.-G.; software, D. J. V.-G.; validation, D. J. V.-G., and L. D. W.; formal analysis, D. J. V.-G.; investigation, D. J. V.-G.; resources, L. D. W.; data curation, D. J. V.-G.; writing—original draft preparation, D. J. V.-G.; writing—review and editing, D. J. V.-G., L. D. W. and M. D. l. C.-G.; visualization, D. J. V.-G.; supervision, L. D. W.; project administration, L. D. W.; funding acquisition, L. D. W. All authors have read and agreed to the published version of the manuscript.

Conflicts of interest

There are no conflicts to declare.

Acknowledgements

LDW acknowledges the support funding provided by the Government of Canada through the Natural Sciences and Engineering Research Council of Canada (NSERC) in the form of a Discovery Grant (RGPIN 04315-2021). The Saskatchewan Structural Sciences Centre (SSSC) is acknowledged for providing facilities to conduct this research. Funding from Canada Foundation for Innovation, NSERC and the University of Saskatchewan to support the research at the SSSC. The technical support provided by Dominic Weninger along with Gopesh Patel is acknowledged. Further, Bernd G. K. Steiger for technical support with XPS analysis is gratefully acknowledged. The authors acknowledge that this work was carried out in Treaty 6 Territory and the Homeland of the Métis. As such, we pay our respect to the First Nations and Métis ancestors of this place and reaffirm our relationship with one another.

Notes and references

1 B. G. K. Steiger and L. D. Wilson, *Chemosphere*, 2024, **349**, 140874.
2 A. Shekhawat, R. Jugade, V. Gomase, S. Kahu, S. Dhandayutham and S. Pandey, *J. Compos. Sci.*, 2023, **7**, 19.
3 S. Pandey, S. Kim, Y. S. Kim, D. Kumar and M. Kang, *Environ. Res.*, 2024, **240**, 117540.
4 N. Morin-Crini, E. Lichtfouse, M. Fourmentin, A. R. L. Ribeiro, C. Noutsopoulos, F. Mapelli, É. Fenyvesi, M. G. A. Vieira, L. A. Picos-Corrales, J. C. Moreno-Piraján, L. Giraldo, T. Sohajda, M. M. Huq, J. Soltan, G. Torri, M. Magureanu, C. Bradu and G. Crini, *Environ. Chem. Lett.*, 2022, **20**, 1333–1375.
5 N. Zaki, N. Hadoudi, A. Charki, N. Bensitel, H. El Ouarghi, H. Amhamdi and M. Ahari, *Sep. Sci. Technol.*, 2023, **58**(3), 1–11.
6 T. A. Aragaw and F. M. Bogale, *Front. Environ. Sci.*, 2023, **11**, 1142227.
7 P. Mahamallik and R. Swain, *Water Sci. Technol.*, 2023, **87**, 3108–3123.
8 B. Nazari, S. Abdolalian and M. Taghavijeloudar, *Environ. Res.*, 2023, **235**, 116595.
9 K. Okaiyeto, U. U. Nwodo, S. A. Okoli, L. V. Mabinya and A. I. Okoh, *Microbiologyopen*, 2016, **5**, 177–211.
10 Y. Hadj Mansour, B. Othmani, F. Ben Rebah, W. Mnif, M. Saoudi and M. Khadhraoui, *Water*, 2023, **15**, 2602.
11 A. K. Badawi, R. S. Salama and M. M. M. Mostafa, *RSC Adv.*, 2023, **13**, 19335–19355.
12 D. J. Venegas-García and L. D. Wilson, *Mater.*, 2022, **15**, 8691.
13 S. Kantipudi and L. Joykutty, *J. Stud. Res.*, 2023, **12**, 1–14.

14 H. K. Agbovi and L. D. Wilson, Chapter 1. Adsorption processes in biopolymer systems: fundamentals to practical applications, in *Natural Polymers-Based Green Adsorbents for Water Treatment*, 2021, pp. 1–53, DOI: 10.1016/B978-0-12-820541-9.00011-9.
15 I. T. S. Kim, V. Sethu, S. K. Arumugasamy and A. Selvarajoo, *J. Water Process Eng.*, 2020, **37**, 101500.
16 B. Tawakkoly, A. Alizadehdakhel and F. Dorosti, *Ind. Crops Prod.*, 2019, **137**, 323–331.
17 F. Madjene, O. Benhabiles, A. Boutra, M. Benchaib and I. Bouchakour, *Int. J. Environ. Sci. Technol.*, 2023, **20**, 12131–12140.
18 O. Dkhissi, A. El Hakmaoui, M. Chatoui, R. Bouyakhsass, H. Bakraouy, T. A. Kurniawan, A. Anouzla, A. Jada and S. Souabi, *Water, Air, Soil Pollut.*, 2023, **234**, 322.
19 A. Skotta, A. Jmiai, W. Elhayaoui, A. El-Asri, M. Tamimi, A. Assabbane and S. El Issami, *J. Taiwan Inst. Chem. Eng.*, 2023, **145**, 104792.
20 S. A. Prabhakar, N. Ojha and N. Das, *Water Sci. Technol.*, 2020, **82**, 2446–2459.
21 A. Benalia, K. Derbal, A. Khalfaoui, R. Bouchareb, A. Panico, C. Gisonni, G. Crispino, F. Pirozzi and A. Pizzi, *Water*, 2021, **13**, 2024.
22 M. Elgegren, J. Nakamatsu, B. Galarreta and S. Kim, *Gels*, 2023, **9**, 847.
23 W. Sriariyakul, T. Swasdisevi, S. Devahastin and S. Soponronnarit, *Food Bioprod. Process.*, 2016, **100**, 391–400.
24 C. Liu, Y. Cui, F. Pi, Y. Cheng, Y. Guo and H. Qian, *Molecules*, 2019, **24**, 1554.
25 D. Kenea, T. Denekew, R. Bulti, B. Olani, D. Temesgen, D. Sefiw, D. Beyene, M. Ebba and W. Mekonin, *S. Afr. J. Chem. Eng.*, 2023, **45**, 294–304.
26 A. Ahmed, *Sohag Eng.*, 2023, **3**, 79–86.
27 M. Getahun, P. Asaithambi, A. Befekadu and E. Alemayehu, *Case Stud. Chem. Environ. Eng.*, 2023, **8**, 100370.
28 L. Bazrafshan, M. Edris and F. K. Mostafapour, *Wulfenia J.*, 2013, **20**, 323–341.
29 D. Kong and L. D. Wilson, *J. Compos. Sci.*, 2020, **4**, 95.
30 S. Anjum, A. Gupta, D. Sharma, D. Gautam, S. Bhan, A. Sharma, A. Kapil and B. Gupta, *Mater. Sci. Eng., C*, 2016, **64**, 157–166.
31 S. D. McConaughy, P. A. Stroud, B. Boudreaux, R. D. Hester and C. L. McCormick, *Biomacromolecules*, 2008, **9**, 472–480.
32 H. K. Agbovi, L. D. Wilson and L. G. Tabil, *Ind. Eng. Chem. Res.*, 2017, **56**, 37–46.
33 N. K. Ibnul and C. P. Tripp, *Talanta*, 2021, **225**, 122023.
34 H. K. Agbovi and L. D. Wilson, *Environ. Chem.*, 2019, **16**, 599.
35 M. H. Mohamed and L. D. Wilson, *Nanomaterials*, 2015, **5**, 969–980.
36 B. G. K. Steiger and L. D. Wilson, *Surfaces*, 2022, **5**, 429–444.
37 Y. Huang, X. Lee, M. Grattieri, F. C. Macazo, R. Cai and S. D. Minteer, *J. Mater. Sci.*, 2018, **53**, 12641–12649.
38 U. A. Edet and A. O. Ifelebuegu, *Processes*, 2020, **8**, 665.
39 N. Fairley, V. Fernandez, M. Richard-Plouet, C. Guillot-Deudon, J. Walton, E. Smith, D. Flahaut, M. Greiner, M. Biesinger, S. Tougaard, D. Morgan and J. Baltrusaitis, *Appl. Surf. Sci. Adv.*, 2021, **5**, 100112.
40 K. V. Naveen, K. Saravanakumar, A. Sathiyaseelan and M.-H. Wang, *Colloid Interface Sci. Commun.*, 2022, **46**, 100566.
41 P. Sun, Y. Ren, J. Zheng and A. Hu, *J. Chem.*, 2019, **2019**, 1–11.
42 T. Y. Hendrawati, R. A. Nugrahani, A. I. Ramadhan, S. Susanty and A. Siswahyu, *IOP Conf. Ser.: Mater. Sci. Eng.*, 2019, **543**, 012014.
43 V. P. Aswathy, A. Bains, K. Sridhar, P. Chawla, M. Sharma, N. Ali, A. Malik and G. Goksen, *Int. J. Biol. Macromol.*, 2024, **267**, 131431.
44 F. I. Gorsi, A. Hussain, T. Kausar, R. Nisar, T. Siddique, S. Yaqub, Sidrah, S. A. Batool and S. Akram, *J. Therm. Anal. Calorim.*, 2024, **149**, 4543–4559.
45 P. Packialakshmi, P. Gobinath, A. Ahamed, H. A. Alodaini, A. A. Hatamleh, M. T. Yassin, A. Idhayadhulla and R. Surendrakumar, *J. Chem.*, 2023, **2023**, 1–14.
46 H.-Y.-Y. Yao, J.-Q. Wang, J.-Y. Yin, S.-P. Nie and M.-Y. Xie, *Food Res. Int.*, 2021, **143**, 110290.
47 S. Das, B. Mishra, K. Gill, M. S. Ashraf, A. K. Singh, M. Sinha, S. Sharma, I. Xess, K. Dalal, T. P. Singh and S. Dey, *Int. J. Biol. Macromol.*, 2011, **48**, 38–43.
48 D. Sharma, A. Sharma, R. Bala and B. Singh, *Int. J. Biol. Macromol.*, 2024, **267**, 131363.
49 J. Irfan, A. Ali, M. A. Hussain, A. Abbas, M. T. Haseeb, M. Naeem-ul-Hassan, I. Azhar, S. Z. Hussain and I. Hussain, *Int. J. Biol. Macromol.*, 2024, **259**, 128879.
50 M. C. Otálora, A. Wilches-Torres and J. A. G. Castaño, *Polymers*, 2021, **13**, 1689.
51 U. Sadiq, H. Gill and J. Chandrapala, *Gels*, 2022, **8**, 597.
52 X.-D. Shi, J.-Y. Yin, X.-J. Huang, Z.-Q. Que and S.-P. Nie, *Int. J. Biol. Macromol.*, 2018, **120**, 2373–2380.
53 X.-D. Shi, J.-Y. Yin, L.-J. Zhang, O.-Y. Li, X.-J. Huang and S.-P. Nie, *Food Hydrocolloids*, 2019, **86**, 50–61.
54 S. Zahmatkesh, M. Karimian, Z. Chen and B.-J. Ni, *J. Environ. Manage.*, 2024, **349**, 119429.
55 Z. Lin, C. Zhang, C. Sun, W. Lu, B. Quan, P. Su, X. Li, T. Zhang, J. Guo and W. Li, *Sep. Purif. Technol.*, 2023, **327**, 124870.
56 L. E. Lan, F. D. Reina, G. E. De Seta, J. M. Meichtry and M. I. Litter, *Water*, 2023, **15**, 1481.
57 S. V. Vargas-Solano, F. Rodríguez-González, R. Martínez-Velarde, S. S. Morales-García and M. P. Jonathan, *Environ. Adv.*, 2022, **7**, 100160.
58 M. A. Inam, R. Khan, D. R. Park, B. A. Ali, A. Uddin and I. T. Yeom, *Minerals*, 2018, **8**, 574.
59 S. Song, A. Lopez-Valdivieso, D. J. Hernandez-Campos, C. Peng, M. G. Monroy-Fernandez and I. Razo-Soto, *Water Res.*, 2006, **40**, 364–372.
60 M. M. T. Khan, K. Yamamoto and M. F. Ahmed, *Water Supply*, 2002, **2**, 281–288.
61 N. K. Asmel, A. R. M. Yusoff, L. Sivarama Krishna, Z. A. Majid and S. Salmiati, *Chem. Eng. J.*, 2017, **317**, 343–355.
62 F. Hesami, B. Bina, A. Ebrahimi and M. Amin, *Int. J. Environ. Health Eng.*, 2013, **2**, 17.
63 M. B. Baskan and A. Pala, *J. Hazard. Mater.*, 2009, **166**, 796–801.

64 B. Perez Mora, S. Bellú, M. F. Mangiameli, M. I. Frascaroli and J. C. González, *J. Water Process Eng.*, 2019, **32**, 100913.
65 H. Kristianto, N. Manurung, I. K. Wardhani, S. Prasetyo, A. K. Sugih and A. A. Arbita, *Water Pract. Technol.*, 2022, **17**, 1332–1346.
66 M. H. Abu Elella, M. W. Sabaa, E. A. ElHafeez and R. R. Mohamed, *Int. J. Biol. Macromol.*, 2019, **137**, 1086–1101.
67 S. N. Tegopoulos, A. Papagiannopoulos and A. Kyritsis, *Phys. Chem. Chem. Phys.*, 2024, **26**, 3462–3473.
68 H. N. Dayarathne, M. J. Angove, R. Aryal, H. Abuel-Naga and B. Mainali, *J. Water Process Eng.*, 2021, **40**, 101820.
69 L. Abramian and H. El-Rassy, *Chem. Eng. J.*, 2009, **150**, 403–410.
70 S. Chaudhary, J. Sharma, B. S. Kaith, S. Yadav, A. K. Sharma and A. Goel, *Ecotoxicol. Environ. Saf.*, 2018, **149**, 150–158.
71 P. E. Ohale, C. E. Onu, N. J. Ohale and S. N. Oba, *Chem. Eng. J. Adv.*, 2020, **4**, 100036.
72 J. Hamman, *Molecules*, 2008, **13**, 1599–1616.
73 A. Mishra, A. Behura, S. Mawatwal, A. Kumar, L. Naik, S. S. Mohanty, D. Manna, P. Dokania, A. Mishra, S. K. Patra and R. Dhiman, *Food Chem. Toxicol.*, 2019, **134**, 110827.
74 J. Shen, L. Zhang, L. Liu, B. Wang, J. Bai, C. Shen, Y. Chen, Q. Fan, S. Chen, W. Wu, X. Feng, L. Wang and W. Huang, *ACS Appl. Mater. Interfaces*, 2019, **11**, 40944–40950.
75 B. Murillo-Amador, M. V. Córdoba-Matson, J. A. Villegas-Espinoza, L. G. Hernández-Montiel, E. Troyo-Diéguez and J. L. García-Hernández, *PLoS One*, 2014, **9**, e94870.
76 J. Li, Z. T. How, C. Benally, Y. Sun, H. Zeng and M. Gamal El-Din, *Sep. Purif. Technol.*, 2023, **313**, 123484.
77 D. J. Venegas-García and L. D. Wilson, *Surfaces*, 2022, **5**, 413–428.
78 J. R. J. R. C. D. Wagner, A. V. Naumkin, A. Kraut-Vass, J. W. Allison and C. J. Powell, *NIST Standard Reference Database 20*, **http:/srdata.nist.gov/xps/**, accessed 22/07/2024.